

Strength differential effect in age hardened aluminum alloys

Jens Kristian Holmen*, Bjørn Håkon Frodal, Odd Sture Hopperstad, Tore Børvik

Structural Impact Laboratory (SIMLab), Department of Structural Engineering, Norwegian University of Science and Technology (NTNU), NO-7491 Trondheim, Norway

Centre for Advanced Structural Analysis (CASA), NTNU, NO-7491, Trondheim, Norway

Abstract

The strength differential (SD) effect, as reported in literature over the past decades, is a discrepancy between the axial stresses in compression and tension. This study investigates the SD effect in aluminum alloys using both experiments and numerical simulations. We present compressive and tensile tests of four aluminum alloys in several tempers with yield strengths varying from 27 MPa to 373 MPa: a total of thirteen different material configurations. The axial stresses measured in compression tests are significantly higher than corresponding tensile stresses for nearly all material configurations. In our tests, the SD effect generally increases with material strength, indicating that aluminum alloys are pressure sensitive. The physical mechanism responsible for the SD effect was not investigated in this paper, but a plasticity model based on the hypothesis that dislocation motion is affected by hydrostatic pressure, as put forth by several authors, gives an accurate description of the material behavior in compression and tension.

Keywords: Experiments, 6xxx aluminum alloys, SD effect, Pressure sensitivity, Drucker-Prager, Stress triaxiality ratio

1. Introduction

For certain metals, the flow stress in compression has been reported to be higher than the flow stress in tension. This difference in strength between compression and tension is called the strength differential (SD) effect and can be defined as

$$SD = 2 \frac{|\sigma_c| - |\sigma_t|}{|\sigma_c| + |\sigma_t|} \quad (1)$$

*Corresponding author. Tel.: +47 930 45 837

Email address: jens.k.holmen@ntnu.no (Jens Kristian Holmen)

where σ_c is the compressive stress and σ_t is the tensile stress. The SD effect was first accounted for in high-strength steels (Hirth and Cohen, 1970; Chait, 1972; Spitzig et al., 1975, 1976). Later, it was also observed in aluminum alloys (Spitzig and Richmond, 1984; Wilson, 2002; Bai and Wierzbicki, 2008). The exact reason for this behavior is to some degree still uncertain. But the finding of the SD effect demonstrated a need to include hydrostatic pressure in plasticity models for metals as for example in the model of Drucker and Prager (1952) where flow stress increases linearly with pressure.

Early accounts of the SD effect in high-strength steels were made by Hirth and Cohen (1970), Chait (1972), and Spitzig et al. (1975, 1976), among others; and later confirmed by for example Singh et al. (2000). What was initially seen as a shortcoming of the compressive test (e.g. friction) was now investigated thoroughly and several hypotheses for the origin of the SD effect were put forth. Some of these hypotheses were systematically reviewed by Hirth and Cohen (1970) and Drucker (1973). Microcracking due to quenching, for example, was dismissed as an explanation since materials that were resistant to microcracking also displayed SD effects. Residual stress resulting from prior deformations, varying cooling temperatures, or phase transformations was examined, but refuted as the main reason for the SD effect since the difference between compression and tension should in this case be wiped out after plastic strains of a few percent. Drucker (1973) further suggested that the stresses used to define the SD effect should be determined after substantial plastic deformation of for instance two or three times the strain at initial yielding. This eliminates contributions from residual stresses and reveals the actual pressure sensitivity of the material. Note that even though residual stresses and microcracking can influence the bulk material behavior and lead to an SD effect for small strains, this is not the same as pressure sensitivity.

In this paper, we use the term SD effect as the discrepancy between measured axial stress in compression and tension tests with the same geometry, while pressure dependence, or pressure sensitivity, is assumed to be the main physical phenomenon responsible for the SD effect. An overestimation of the axial stress in pre-notched tension tests using the pressure independent von Mises yield surface can also indicate pressure dependence of the material being simulated although this overestimation might also be explained by void growth or plastic anisotropy as will be discussed later.

Spitzig and Richmond (1984) conducted compression and tension tests of aluminum alloy AA1100 under superimposed hydrostatic pressure. Superimposing hydrostatic pressure can increase ductility and is utilized in metal forming (Peng et al., 2009; Wu et al., 2009). However, it was applied by Spitzig and

Richmond (1984) to reduce the influence of anisotropy, inhomogeneity, residual stresses, specimen geometry, and Bauschinger effects, thus helping to isolate the true pressure sensitivity of the material. The data for aluminum was presented along with previously obtained data for steel (Spitzig et al., 1975, 1976) and the authors concluded that flow stress is sensitive to superimposed hydrostatic pressure, but that the magnitude of the SD effect is not. They found a linear relationship between equivalent stress $\sigma_{\text{eq}} = \sqrt{3J_2}$ and hydrostatic pressure P on the form

$$\sigma_{\text{eq}} = \sigma_0 (1 + 3\alpha P). \quad (2)$$

Here the hydrostatic pressure P is defined as

$$P = -\frac{I_1}{3} = -\frac{\sigma_{kk}}{3} = -\frac{\sigma_1 + \sigma_2 + \sigma_3}{3} \quad (3)$$

where I_1 is the first invariant of the stress tensor and σ_1 , σ_2 , and σ_3 are the principal stresses. Further, $J_2 = 1/2\sigma'_{ij}\sigma'_{ij}$ is the second invariant of the deviatoric stress tensor ($\sigma'_{ij} = \sigma_{ij} + P\delta_{ij}$), σ_0 is the value of σ_{eq} at zero hydrostatic pressure (1 atm), and α is a pressure coefficient which they found to be about 19.2 TPa^{-1} for all iron-based materials. For aluminum, they suggested a pressure coefficient of 56.0 TPa^{-1} . These values, which are in accordance with dislocation models (Spitzig and Richmond, 1984), imply that α is a function of the lattice structure, and thus that the SD effect is a manifestation of the effect of pressure on dislocation motion. Further, they discovered that an associated flow rule severely overestimates the volume changes when using a pressure dependent yield surface, so a non-associative flow rule is needed when modeling pressure sensitive metals. Atomistic simulations by Bulatov et al. (1999) later confirmed that pressure dependence of aluminum is not associated with volume expansion and that it is, indeed, a result of the effect of pressure on dislocation motion.

More recently, Bai and Wierzbicki (2008) presented a large experimental and numerical study on the behavior of aluminum alloy AA2024-T351. They conducted various compressive and tensile experiments that revealed an SD effect that likely derives from pressure dependence. The plastic behavior was also found to be sensitive to the third deviatoric stress invariant $J_3 = \det(\sigma'_{ij})$. The authors obtained excellent results when modeling pressure sensitivity similar to Eq. (2) with a non-associative flow rule, and by incorporating the effect of J_3 they managed to model plane strain tests as well. Later, Gao et al. (2009) investigated the

effects of stress state on plasticity of aluminum alloy AA5083-H116 by using various tension specimens, but no compression specimens. Thus, they only found a small pressure sensitivity. However, just like in the tests of [Bai and Wierzbicki \(2008\)](#), the effect of J_3 was significant. [Seidt and Gilat \(2013\)](#) confirmed that aluminum alloy AA2024-T351 is both pressure sensitive and J_3 dependent. They reported an SD effect of 4%.

[Wilson \(2002\)](#) presented tension experiments on smooth and notched specimens and showed that the pressure independent von Mises yield surface overestimated the axial stress of the notched specimens. The pressure dependent model of [Drucker and Prager \(1952\)](#) was on the other hand capable of predicting the correct stress level. [Guo et al. \(2008\)](#) applied Gurson's homogenization to obtain a constitutive model for voided materials with a pressure sensitive matrix material. [Yoon et al. \(2014\)](#) put forth a general anisotropic yield function where the difference between the tensile and compressive strengths can be incorporated either through a linear pressure dependence or through J_3 -dependence. Due to the linear pressure dependence, this model is consistent with the results of [Spitzig and Richmond \(1984\)](#).

The desire to predict the behavior of anisotropic metal sheets seems to be the main catalyst for the interest in the SD effect. Models that account for this phenomenon, regardless of its physical cause, have been proposed by for instance [Brüning \(1999\)](#), [Stoughton and Yoon \(2004\)](#), [Kuroda \(2004\)](#), [Gao et al. \(2011\)](#), [Lou et al. \(2013\)](#), [Smith et al. \(2013\)](#), and [Kleiser et al. \(2015\)](#). A discrepancy between the stress levels in compression and tension is often identified in tests of hexagon-closed packed (HCP) metals where plastic deformation occurs not only by slip, but also by twinning ([Hosford and Allen, 1973](#)). This is the case for titanium (e.g., [Nixon et al., 2010](#); [Tuninetti et al., 2015](#)) and magnesium alloys (e.g., [Cazacu and Barlat, 2004](#); [Habib et al., 2017](#)). To this end, [Cazacu and Barlat \(2004\)](#) presented a model that is capable of capturing the SD effect due to direction-sensitive twinning. For magnesium alloys the compressive strength is commonly lower than the tensile strength and the yield locus is often highly anisotropic. This type of SD effect is not addressed in the current study.

This study is mainly experimental and reveals the possible intrinsic pressure dependence of age hardened aluminum alloys. We present compressive and tensile test data for four different age hardened aluminum alloys in several different tempers. Almost all the tempers exhibit an SD effect. We demonstrate the inability of the pressure independent von Mises yield surface to describe this behavior. Based on the work of [Spitzig and Richmond \(1984\)](#), we presume that hydrostatic pressure affects the dislocation motion and we use a pressure dependent non-associative Drucker-Prager plasticity model to simulate the tests. The

Table 1: Chemical composition of the aluminum alloys considered in this study (in wt-%).

Alloy	Si	Mg	Mn	Cu	Fe	Cr	Ti	Al
6060	0.42	0.47	0.02	<0.01	0.19	<0.01	<0.01	Balance
6070	1.38	1.23	0.54	0.26	0.22	<0.01	<0.01	Balance
6082.25	0.88	0.60	0.53	0.02	0.18	0.15	0.01	Balance
6082.50	1.02	0.67	0.54	<0.01	0.20	<0.01	<0.01	Balance

work contributes experimental evidence that age hardened aluminum alloys exhibit an SD effect, and the numerical simulations suggest that the observed SD effect can be attributed to pressure sensitivity of dislocation motion. The intention of this work was not to propose a new model for the SD effect, but to show that it exists and can be important for age hardened aluminum alloys.

2. Material

Four aluminum alloys, all delivered by Hydro Aluminium, were investigated in this study: AA6060, AA6070, AA6082.25, and AA6082.50. The chemical compositions can be found in Table 1. The alloys were heat treated to tempers O (annealed), T6 (peak strength), and T7 (over aged). Additional data for temper T4 (naturally aged) of AA6070 will also be presented. Figure 1 shows the flow stress curves represented by an extended Voce hardening rule for all configurations. Processing routes and aging heat treatments are summarized below.

AA6070 was provided as 20 mm thick hot-rolled plates. All the plates were direct chill (DC) cast to a thickness of 126 mm, machined to 103 mm, homogenized at 550 °C for 4 h, and then hot-rolled to the ultimate thickness of 20 mm. Solution heat treatment took place at 560 °C for 90 min before the plates were instantly water-quenched leaving the plates in the T4 condition. Subsequent artificial aging to obtain temper T6 was 64 h at 160 °C before slow cooling, while temper T7 required 8 h at 200 °C before slow cooling. Temper O was held for 24 h at 350 °C before slow cooling; this extended heat treatment was considered sufficient to obtain the soft state regardless of the solution heat treatment. Test specimens were extracted after aging for this alloy. All the data we present for AA6070 comes from specimens oriented along the rolling direction of the plate since it is the most ductile orientation.

AA6060, AA6082.25, and AA6082.50 were delivered as rectangular extruded profiles. These alloys were first cast into billets with a diameter of 200 mm, then extruded to rectangular profiles with a thickness of 10 mm and a width of 83 mm, before they were homogenized using industrial practice. Test specimens

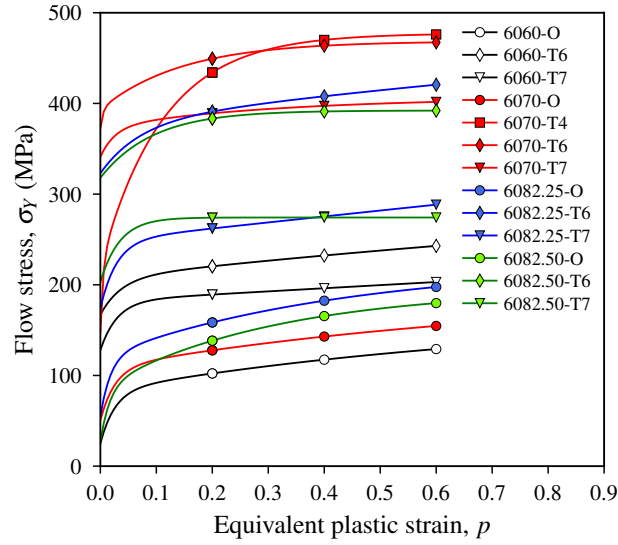


Figure 1: Flow stress curves represented by an extended Voce hardening rule (Eq. (18)) from uniaxial tension tests for the materials in this study. Note that the curve for 6070-T4 is from a uniaxial compression test.

were extracted from these profiles prior to the subsequent aging heat treatment. After solution heat treatment at 540 °C for 15 min the specimens were instantly water-quenched. Temper O was held at 350 °C for 24 h, temper T6 was held at 185 °C for 5 h, while T7 required 185 °C for one week. All the data we present for these three alloys come from specimens oriented transversely to the extrusion direction of the profile. This was done to minimize the scatter due to possible spatial variations in material properties over the cross section of the extruded profile.

The AA6060 alloy has a strong cube texture with a minor Goss component. It is recrystallized and the grains are equiaxed with an average size between 60 μm and 70 μm. AA6070 exhibits a rotated cube texture. The grains are elongated in the rolling direction and they can be several mm long while being between 0.5 mm and 1 mm in the plane perpendicular to the rolling direction. This structure is also recrystallized. The AA6082.25 alloy has fibrous grain structure and displays cube texture with components along the β-fibre. The grains are several mm long in the extrusion direction (ED), about 10 μm in the thickness direction (ND), and about 150 μm in the transverse direction (TD) of the profile; they contain sub-grains approximately 2 μm to 10 μm in diameter with low-angle grain boundaries. AA6082.50 is recrystallized and exhibits a rotated cube texture. The grains are elongated along the ED and are several mm long and between 300 μm and 400 μm wide. More information regarding the AA6060, AA6082.25, and AA6082.50 alloys can be found in [Khadyko et al. \(2014\)](#) and [Frodal et al. \(2017\)](#), while further details about AA6070 can be found

in [Johnsen et al. \(2013\)](#) and [Holmen et al. \(2013, 2016\)](#).

3. Mechanical tests

3.1. Test program

We present results from four types of mechanical tests in this study: Uniaxial tension tests on smooth cylindrical specimens (Figure 2a), uniaxial compression tests on right cylindrical upsetting specimens (Figure 2b), and tension and compression tests on pre-notched diabolo specimens (Figure 2c). Uniaxial compression tests were only conducted on AA6070. Table 2 summarizes the experimental program. Three to twelve repetitions were done of each test, allowing us to evaluate the repeatability of the experimental setups. No effort was made to determine the volume change of the materials during the experiments.

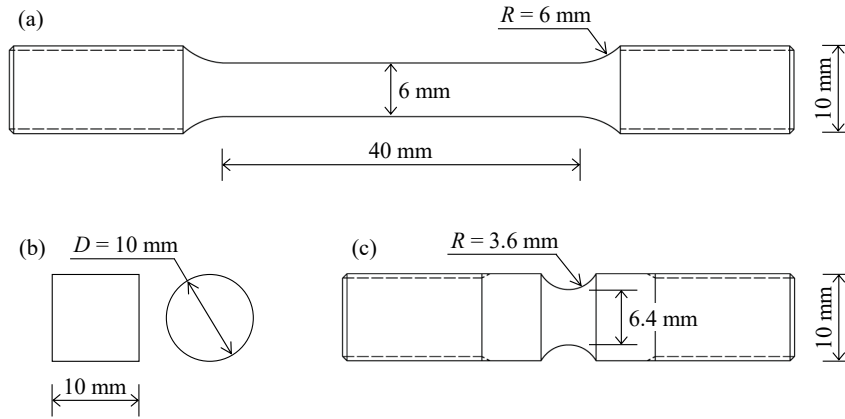


Figure 2: Geometries of the cylindrical test specimens: (a) Uniaxial tension specimen, (b) upsetting specimen, and (c) pre-notched diabolo specimen.

The stress state in the tests can be conveniently described by the dimensionless stress triaxiality ratio T and Lode parameter L_μ . The stress triaxiality ratio is related to I_1 and defined by

$$T = \frac{I_1}{3\sqrt{3}J_2} = -\frac{P}{\sqrt{3}J_2}. \quad (4)$$

The Lode parameter L_μ which is related to J_3 and thus describes the deviatoric state of the material is defined in terms of the principal stresses ($\sigma_1 \geq \sigma_2 \geq \sigma_3$) as

$$L_\mu = \frac{2\sigma_2 - \sigma_1 - \sigma_3}{\sigma_1 - \sigma_3}. \quad (5)$$

Table 2: Overview of the experimental tests.

Configuration	Uniaxial tension	Upsetting compression	Diabolo tension	Diabolo compression
6060-O	X		X	X
6060-T6	X		X	X
6060-T7	X		X	X
6070-O	X	X	X	X
6070-T4	X	X	X	X
6070-T6	X	X	X	X
6070-T7	X	X	X	X
6082.25-O	X		X	X
6082.25-T6	X		X	X
6082.25-T7	X		X	X
6082.50-O	X		X	X
6082.50-T6	X		X	X
6082.50-T7	X		X	X

Due to the axisymmetric nature of the test specimens in this study, the Lode parameter L_μ equals -1 for all the tension tests and 1 for all the compression tests. The stress triaxiality ratio T varies during tests, but the initial value T_0 can be roughly estimated by the Bridgman formula (Bridgman, 1952; Hancock and Mackenzie, 1976)

$$T_0 = \pm \left(\frac{1}{3} + \ln \left(1 + \frac{a_0}{2R} \right) \right) \quad (6)$$

where R is the radius of curvature of the neck, and a_0 is the minimum cross-section radius of the specimen. A positive sign is used for tension tests while a negative sign is used for compression tests. As expected, $T_0 = 0.33$ for the uniaxial tension specimen and $T_0 = -0.33$ for the uniaxial compression specimen. Eq. 6 estimates $T_0 \approx 0.70$ for the pre-notched diabolo specimens tested in tension and $T_0 \approx -0.70$ for pre-notched diabolo specimens tested in compression which correspond well with results from numerical simulations.

3.2. Uniaxial tension tests

Figure 3 shows typical true stress-strain curves until necking for cylindrical specimens of aluminum alloy AA6070. Their initial diameter was 6 mm (Figure 2a). We conducted the tests in a hydraulic testing machine at an initial strain rate of 5×10^{-4} 1/s. A laser micrometer continuously measured the diameters D_{\perp} in the transverse direction of the specimen and D_t in the thickness direction of the component (Fourmeau et al., 2011; Frodal et al., 2017). By using the force measurements F from a calibrated load cell and the diameter measurements we calculated the axial component of the Cauchy stress (σ_{11}) and the logarithmic strain ($\varepsilon_l = \varepsilon_{11}$), both averaged over the cross-section area, as

$$\sigma_{11} = \frac{F}{A}, \quad \varepsilon_{11} = \ln \frac{A_0}{A} + (1 - 2\nu) \frac{\sigma_{11}}{E}, \quad (7)$$

where plastic incompressibility was assumed. The current cross-section area of the test specimen is given by

$$A = \frac{\pi D_{\perp} D_t}{4}, \quad (8)$$

and $A_0 = \pi D_0^2/4$ is the initial cross-section area of the test specimen. Young's modulus and Poisson's ratio for aluminum are taken as $E = 70,000$ MPa and $\nu = 0.3$, respectively. Note that we assume that the cross section is elliptical during deformation. Only results from the rolling direction are reported here, but tests with their loading axis oriented 45° and 90° with respect to the rolling direction were also conducted for AA6070 in uniaxial tension and uniaxial compression. The orientation had little effect on the stress level, but in tension tests the fracture strains were significantly lower in the 45° and 90° directions compared to the rolling direction. This is, however, not the focus of this study and more information can be found in Holmen et al. (2013, 2016).

The uniaxial tension tests conducted on AA6070 were done more than two years prior to the rest of the tests. This means that temper T4 experienced additional aging after the tensile testing and was, thus, not fully developed when those tests were conducted. Therefore, the uniaxial tension tests cannot be directly compared to the upsetting tests for AA6070-T4 as will be commented on below. The other alloys (AA6060, AA6082.25, and AA6082.50) were also tested in uniaxial tension, but these results were solely used to calibrate the hardening curves for numerical simulations.

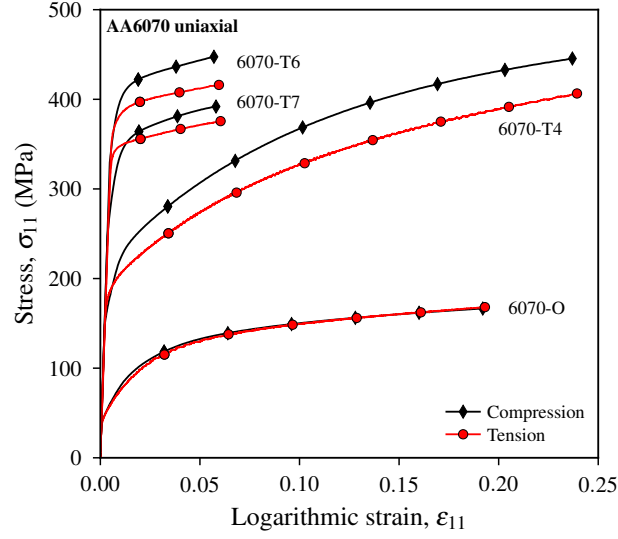


Figure 3: True stress-strain curves from the uniaxial tension and compression tests for aluminum alloy AA6070 plotted until point of necking in the tension tests.

3.3. Uniaxial compression (upsetting) tests

In addition to the tension data, Figure 3 shows true stress-strain curves for upsetting tests on the four different tempers of AA6070. They were conducted on right cylinders with both height and diameter equal to 10 mm (Figure 2b). During testing the cylinders were compressed between two hardened steel platens at an initial strain rate of 5.0×10^{-4} 1/s. We applied graphite paste to the machine-specimen interfaces to reduce the effects of friction. The force F was measured by a calibrated load cell while two MTS extensometers measured the displacement on diametrically opposite sides of the cylinders. The longitudinal true stress-strain curves for the upsetting tests were found as

$$\sigma_{11} = \frac{F}{A} = \frac{4FL}{\pi D_0^2 L_0}, \quad \varepsilon_{11} = \ln \frac{L}{L_0} \quad (9)$$

where L is the length, L_0 is the initial length, and D_0 is the initial diameter of the specimens. Plastic incompressibility and negligible elastic strains were assumed to calculate the stress. Eq. (9) also assumes frictionless machine-specimen interfaces, although friction is nearly impossible to eliminate completely. The curves are plotted in the same quadrant as the tensile tests to simplify the comparison.

3.4. Pre-notched diabolo tension and compression tests

Pre-notched diabolo specimens (Figure 2c) of all configurations were tested both in tension and compression using the same setup as for uniaxial tension tests in Section 3.2. The initial notch radius R was 3.6 mm and the minimum initial cross-section diameter was 6.4 mm. Eq. (8) was used to find the current area based on the two continuously measured perpendicular diameters D_{\perp} and D_{\parallel} . The true stress-strain curves shown for all configurations in Figure 4 were determined as

$$\sigma_{11} = \frac{F}{A}, \quad \varepsilon_{11} = \ln \frac{A_0}{A} \quad (10)$$

where we have assumed both negligible elastic strains and plastic incompressibility. As in Figure 3, all the curves in Figure 4 are shown in the tensile quadrant to simplify comparison between compression and tension results. The true stress-strain curves for the pre-notched diabolo specimens were plotted until a logarithmic strain of 0.1 unless failure occurred earlier.

4. Experimental results

Representative results from tests on the uniaxial tension specimen and cylindrical upsetting specimen in Figure 2a and b, respectively, are shown in Figure 3. This set of tests was only obtained for aluminum alloy AA6070. Temper O seemingly exhibits no SD effect, while axial stresses in compression are noticeable higher than the axial stresses in tension for tempers T6 and T7, even at substantial strains, confirming that residual stress is not the cause. The SD effect in temper T4 is exaggerated due to natural aging, and the results are viewed as qualitative at best. The SD effects calculated from the measured axial stress σ_{11} after a logarithmic strain of 0.02 using Eq. (1) are listed in Table 3. Disregarding temper T4, the data could suggest that friction affects the results from the upsetting tests. However, friction cannot account for the main part of the discrepancy between compressive and tensile behavior, as will be seen in the following.

Figure 4 shows the true stress-strain curves from tests of all the material configurations with the pre-notched diabolo specimens in Figure 2c. One representative curve is shown from each data set. Table 4 summarizes the test data and shows the measured axial stress σ_{11} at a logarithmic strain of 0.02 along with the SD effect calculated by Eq. (1). The scatter is indicated by the columns listing maximum, average, and minimum SD effect. The maximum SD effect was calculated based on the tension test with the lowest axial stress and the compression test with the highest axial stress. The minimum SD effect was calculated based

Table 3: SD effect and the measured axial tensile stress for uniaxial tests on AA6070. The listed values are taken at a logarithmic strain of 0.02.

Configuration	σ_{11}	SD effect
6070-O	99 MPa	4.0%
6070-T4*	226 MPa	11.3%
6070-T6	397 MPa	6.3%
6070-T7	356 MPa	2.5%

*Note that the listed SD effect for T4 is exaggerated due to natural aging.

Table 4: Summary of experimental test data from the pre-notched diabolo compression and tension tests. All the values are taken at a logarithmic strain of 0.02. The SD effect is calculated directly from the measured axial stress while β is calculated from the Bridgman corrected stress ($\bar{\sigma}_T$). The measured axial stress σ_{11} from the pre-notched diabolo tensile tests is shown to illustrate the strength of the material.

Configuration	σ_{11} (Test)	SD effect			β		
		Max.	Avg.	Min.	Max.	Avg.	Min.
6060-O	73 MPa	6.8%	5.3%	4.0%	5.9°	4.6°	3.0°
6060-T6	250 MPa	7.2%	3.1%	0.2%	6.3°	2.7°	0.1°
6060-T7	200 MPa	7.6%	5.6%	3.7%	6.4°	4.8°	2.9°
6070-O	124 MPa	0.4%	-0.3%	-1.2%	0.0°	-0.4°	-1.0°
6070-T4	326 MPa	4.0%	3.4%	2.9%	3.4°	3.0°	2.4°
6070-T6	525 MPa	6.9%	6.1%	5.4%	6.0°	5.2°	4.6°
6070-T7	465 MPa	4.4%	3.6%	2.5%	3.9°	3.3°	2.3°
6082.25-O	123 MPa	3.0%	1.5%	0.2%	2.6°	1.3°	0.0°
6082.25-T6	423 MPa	5.7%	4.5%	3.1%	4.7°	3.7°	2.5°
6082.25-T7	256 MPa	3.5%	2.8%	1.9%	2.9°	2.4°	1.7°
6082.50-O	88 MPa	9.0%	4.4%	-2.1%	8.1°	3.7°	-2.1°
6082.50-T6	436 MPa	9.1%	6.3%	3.9%	7.9°	5.5°	3.3°
6082.50-T7	294 MPa	8.7%	6.0%	4.0%	7.2°	5.2°	3.5°

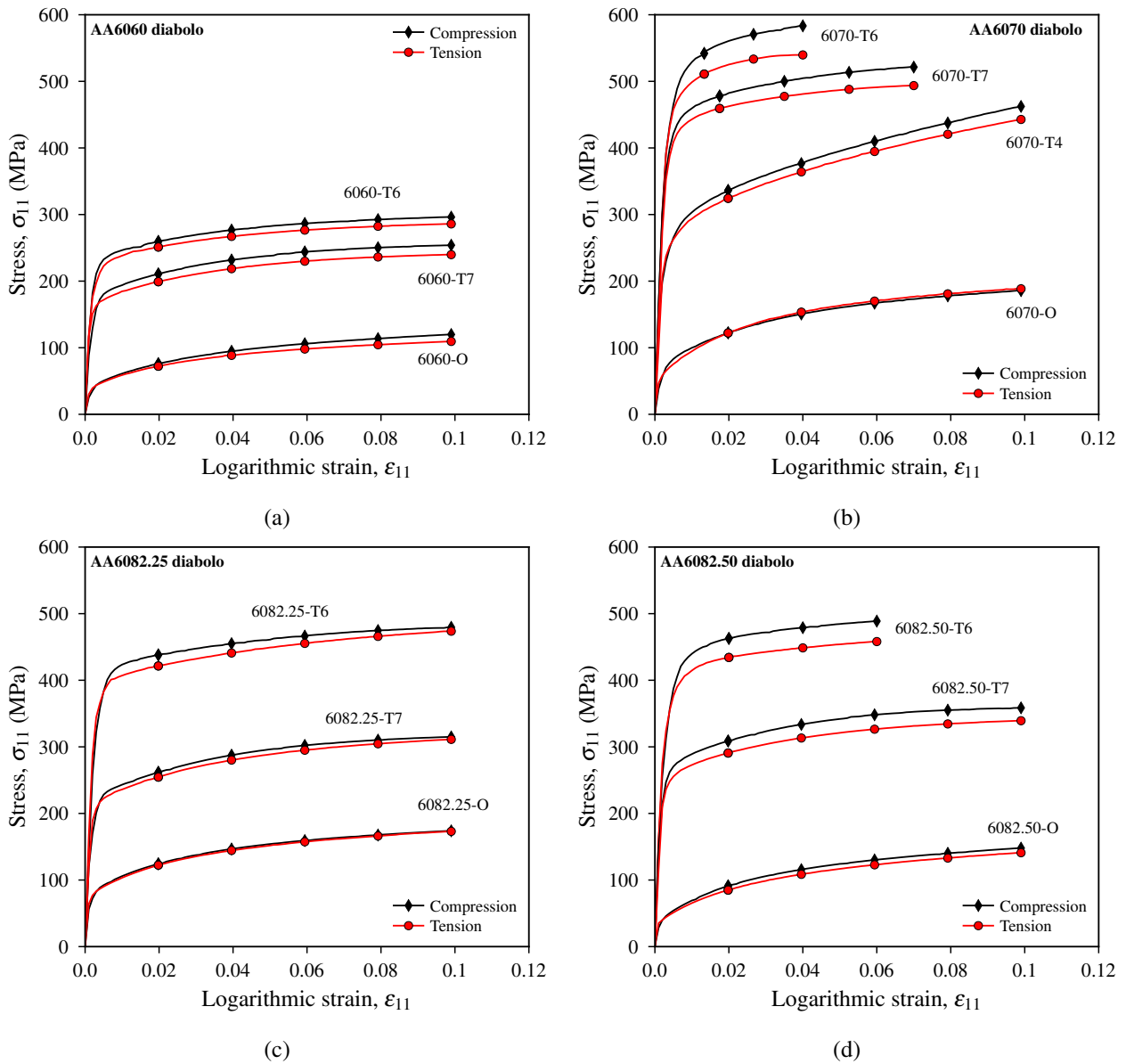


Figure 4: Representative true stress-strain curves from the pre-notched diablo tension and compression tests for aluminum alloy (a) 6060, (b) 6070, (c) 6082.25, and (d) 6082.50.

on the tension test with the highest axial stress and the compression tests with the lowest axial stress. The average SD effect was calculated based on the average stress from all the tension tests and the average stress from all the compression tests. The scatter is significant for some of the configurations; however, the overall trend shows that the SD effect increases with the axial stress.

Figure 5 illustrates the evolution of the maximum, average, and minimum SD effect from the pre-

Table 5: Lankford coefficients in tension and compression from the pre-notched diabolo tests.

Configuration	Tension	Compression
6060-O	1.24	1.40
6060-T6	1.27	1.36
6060-T7	1.24	1.27
6070-O	0.79	0.79
6070-T4	0.81	0.84
6070-T6	0.69	0.77
6070-T7	0.76	0.84
6082.25-O	0.82	0.85
6082.25-T6	0.97	0.95
6082.25-T7	0.85	0.83
6082.50-O	0.45	0.51
6082.50-T6	0.36	0.55
6082.50-T7	0.41	0.59

notched diabolo specimens for all alloys in T6 temper. SD effect is calculated from the measured axial stress σ_{11} using Eq. (1). The scatter for AA6060-T6 is large and the magnitude of the SD effect lies somewhere between -2% and 8%. This is mainly due to spread in the compression tests. AA6070-T6 exhibits less scatter, and the SD effect lies between 4% and 8%; here it increases slightly with the strain. For AA6082.25-T6, the scatter is moderate and the SD effect decreases with straining. [Frodal et al. \(2017\)](#) observed internal buckling of the elongated grains under large compressive strains which might explain why the SD effect decreases with increasing strain for this particular configuration. For AA6082.50-T6 the SD effect varies between around 4% and 10% and it hardly changes with the strain.

Measuring two perpendicular diameters through the tests allowed us to calculate the Lankford coefficients for the thirteen material configurations. They are shown in Table 5. The Lankford coefficient is the ratio between the two transverse strains, which for AA6060, AA6082.25, and AA6082.50 is the ratio between the incremental strains in the extrusion direction (ED) and thickness direction (ND) of the extrusion. For AA6070 it is the ratio between the incremental strain transverse to the rolling direction and the incremental strain in the thickness direction of the plate. The Lankford coefficients for all materials are different from unity. This indicates plastic anisotropy which was expected from the crystallographic textures of these materials. In some cases, the Lankford coefficients have different values in tension and compression.

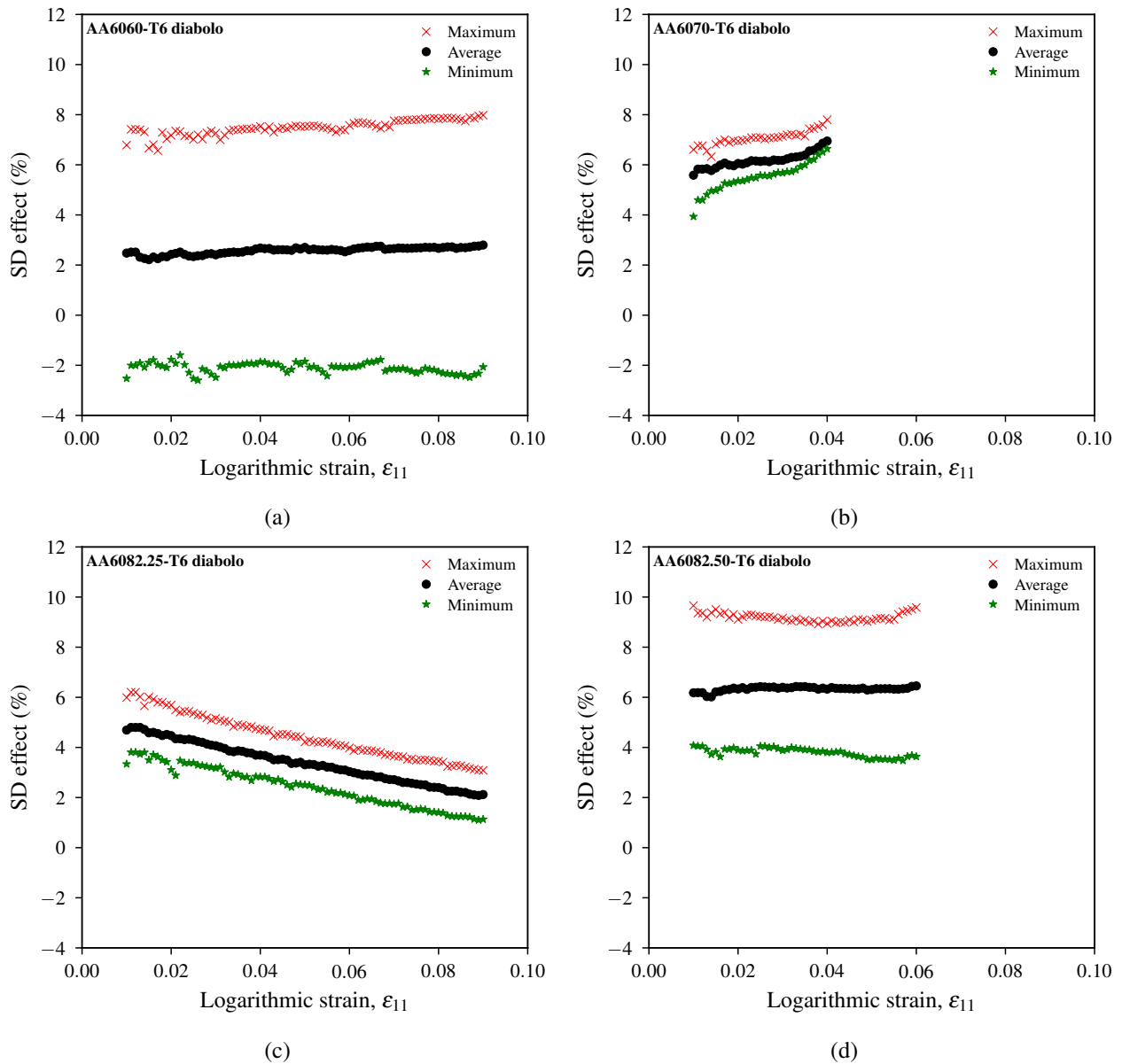


Figure 5: Evolution of the SD effect in the pre-notched diabolo tests from the T6 temper of (a) 6060, (b) 6070, (c) 6082.25, and (d) 6082.50. Note that the SD effect is calculated based on the axial stress σ_{11} measured in the tests.

5. Numerical simulations

There are two reasons for conducting the numerical simulations in this study: (1) to evaluate if the specimen geometry and boundary conditions contributed to the observed SD effect; and (2) to investigate if the hypothesis of [Spitzig and Richmond \(1984\)](#) about pressure sensitivity of the dislocation motion can describe the SD effect. Simulations with both a pressure independent plasticity model and a pressure de-

pendent plasticity model are presented in the following. Note that the pressure sensitivity of the model in Section 5.2 is not calibrated from our experimental data but based on the results of [Spitzig and Richmond \(1984\)](#).

5.1. Pressure independent plasticity modeling

The pressure independent von Mises yield surface is first used to simulate the tests. The von Mises model assumes volume conserving and pressure independent plasticity (Figure 6) which is customary when modeling metals. Further, the yield surface is a circle in the deviatoric plane, and thus a cylinder in the principal stress space. This means that the plastic behavior is a function of the second deviatoric invariant J_2 , hence the name J_2 -plasticity. The von Mises yield criterion reads

$$f(\sigma_{ij}, p) = \sqrt{3J_2} - \sigma_Y = 0 \quad (11)$$

where σ_Y is the quasi-static flow stress that can be determined from a simple material test. As is common, an associative flow rule is used and the plastic rate-of-deformation tensor is defined by

$$D_{ij}^p = \lambda \frac{\partial f}{\partial \sigma_{ij}} \quad (12)$$

where λ is the plastic multiplier. Associative flow implies that the plastic strain increment is normal to the yield surface and it is often referred to as the normality rule.

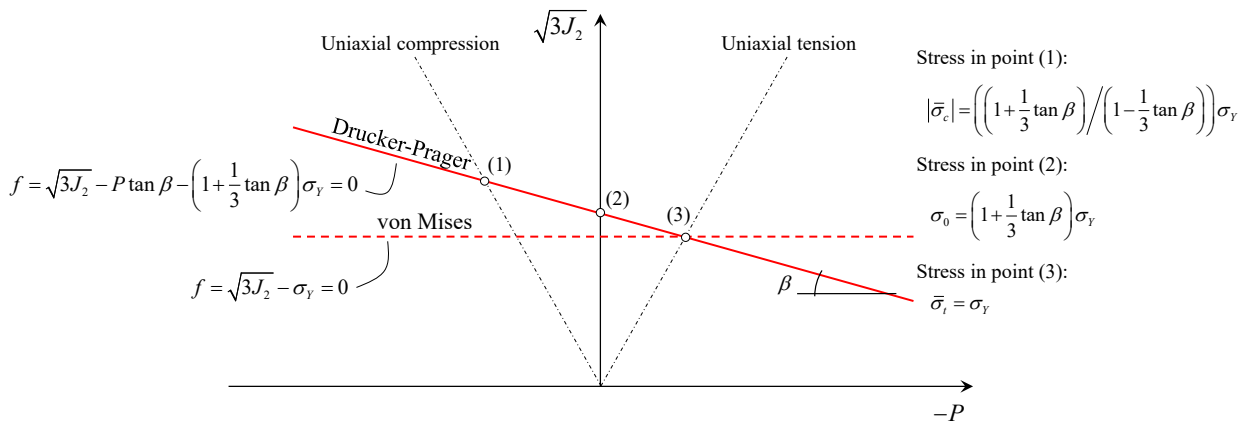


Figure 6: Geometric representation of the von Mises (dashed red line) and the Drucker-Prager (solid red line) yield surfaces.

5.2. Pressure dependent plasticity modeling

We also applied the yield surface proposed by [Drucker and Prager \(1952\)](#) to simulate the various tests. This is an isotropic and pressure dependent model where the deviatoric strength increases with increasing pressure. The Drucker-Prager yield criterion is a right circular cone in the principal stress space shown in the $\sqrt{3}J_2 - P$ -plane in [Figure 6](#). It can conveniently be defined as ([Abaqus Documentation, 2014](#))

$$f(\sigma_{ij}, p) = \sqrt{3}J_2 - P \tan \beta - \left(1 + \frac{1}{3} \tan \beta\right) \sigma_Y = 0 \quad (13)$$

where β is the friction angle that controls the pressure sensitivity of the material. The pressure independent von Mises yield criterion is obtained by setting $\beta = 0$. Note that with this formulation of the criterion σ_Y is the quasi-static flow stress in tension.

As put forth by [Bridgman \(1952\)](#), [Spitzig and Richmond \(1984\)](#), [Bulatov et al. \(1999\)](#), and others, plastic deformation of metals should be volume conserving. For a pressure sensitive yield surface as the one in [Eq. \(13\)](#), the associative flow rule predicts significant volume changes. We therefore assume non-associated plastic flow. The plastic flow rule now reads

$$D_{ij}^p = \lambda \frac{\partial g}{\partial \sigma_{ij}} \quad (14)$$

where $g \geq 0$ is the plastic flow potential which is different from the yield function f . Volume conservation is obtained by using the same plastic potential function as in J_2 flow theory, i.e., $g = \sqrt{3}J_2$. In [Abaqus/Standard](#), which is used in this study, this particular isotropic and volume conserving version of the Drucker-Prager criterion can be obtained by setting the flow stress ratio K to 1.0 and the dilatation angle ψ to 0.0. The friction angle β can be determined from uniaxial tension and compression tests as

$$\beta = \tan^{-1} \left(3 \frac{|\bar{\sigma}_c| - |\bar{\sigma}_t|}{|\bar{\sigma}_c| + |\bar{\sigma}_t|} \right) \quad (15)$$

where the bar denotes uniaxial values, i.e., $\bar{\sigma}_t$ is the stress in uniaxial tension and $\bar{\sigma}_c$ is the stress in uniaxial compression. Note that β is presented in degrees and that [Eq. \(15\)](#) has solely been used to evaluate the numerical results in this paper, nothing else.

As outlined previously, we assume that the conjecture of [Spitzig and Richmond \(1984\)](#) is correct, which means that the pressure coefficient α is a material constant and that it can be used in the calibration of the non-associated Drucker-Prager plasticity model. By choosing α as 56.0 TPa^{-1} we can calculate the appropriate value of the friction angle β for numerical simulations as

$$\alpha = \frac{\tan \beta}{(3 + \tan \beta)\bar{\sigma}_t} \Leftrightarrow \beta = \tan^{-1} \left(\frac{3\alpha\bar{\sigma}_t}{1 - \alpha\bar{\sigma}_t} \right) \quad (16)$$

which was found by combining Eq. (2) and Eq. (13). The magnitude of β depends on the stress and is not constant for work hardening materials. Evolution of β with work hardening is not accounted for in this study.

[Spitzig et al. \(1976\)](#) pointed out that in a simple case of uniaxial compression or tension, $I_1 = \bar{\sigma}$ and $\sqrt{3J_2} = |\bar{\sigma}|$, where $\bar{\sigma}$ is the uniaxial stress in either tension or compression with tension being positive. In a uniaxial state which for example exists in a smooth tensile specimen before necking or in an upsetting test with no barreling, $\bar{\sigma}$ is equal to the measured axial stress σ_{11} . However, most of our tests were conducted using pre-notched diabolo specimens. In such tests the magnitude of the average axial stress is higher than it would have been in the uniaxial condition due to hydrostatic stress introduced by the notch. We can compensate for the hydrostatic stress by following Bridgman's mathematical analysis ([Bridgman, 1944](#)). According to Bridgman, the uniaxial stress $\bar{\sigma}$ that would exist in the test without the tri-axial stresses introduced by the notch is

$$\bar{\sigma} = \frac{\sigma_{11}}{\left(1 + \frac{2R}{a_0}\right) \ln \left(1 + \frac{a_0}{2R}\right)}. \quad (17)$$

As in Eq. (6), R is the radius of curvature of the neck, and a_0 is the radius of the minimum cross section of the specimen. For the pre-notched diabolo specimens in Figure 2c, $R = 3.6 \text{ mm}$ and $a_0 = 3.2 \text{ mm}$.

The results from the pre-notched diabolo tension tests were scaled with Eq. (17) to approximate the uniaxial flow stress. By using Eq. (16) we could then estimate the Drucker-Prager friction angle of all the material configurations. The results are summarized in Table 6, where β is the angle of friction (in degrees) and $\bar{\sigma}_t$ is the Bridgman corrected (compensated for the triaxial stress state) tensile stress at a logarithmic strain of 0.02. Keep in mind that there are several assumptions that are required for the Bridgman correction to be valid, all of which are not strictly fulfilled here ([Dieter, 1988](#)). However, the Bridgman analysis was

Table 6: The friction angle β estimated from Eq. (16) which is used as input in the numerical simulations. The listed stress $\bar{\sigma}_t$ is the Bridgman corrected tensile stress taken from the diabolo tests at a logarithmic strain of 0.02.

Configuration	$\bar{\sigma}_t$ (Bridgman)	β
6060-O	61 MPa	0.7°
6060-T6	209 MPa	2.2°
6060-T7	167 MPa	1.7°
6070-O	104 MPa	1.2°
6070-T4	273 MPa	3.0°
6070-T6	439 MPa	4.3°
6070-T7	389 MPa	3.9°
6082.25-O	103 MPa	1.2°
6082.25-T6	354 MPa	3.5°
6082.25-T7	214 MPa	2.2°
6082.50-O	73 MPa	0.9°
6082.50-T6	364 MPa	3.6°
6082.50-T7	246 MPa	2.5°

necessary to use the data from pre-notched diabolo tests, both to calculate β from the experimental tests with Eq. (15), and to estimate β with the pressure sensitivity parameter from [Spitzig and Richmond \(1984\)](#) with Eq. (16).

5.3. Finite element models

All the simulations reported in this paper are run with [Abaqus/Standard](#). We exploit the inherent symmetry of all the test specimens and apply axisymmetric boundary conditions. The finite element models are shown in Figure 7. Only the upper half of the uniaxial tension and pre-notched diabolo specimens were modeled. In the model of the upsetting test, we included the entire height of the specimen, but we neglected friction. Since the machine-specimen interfaces are not completely frictionless, the compressive stresses in the simulations will be slightly underestimated. However, the correct experimental trends cannot be predicted by merely including friction in the simulations, indicating that the effects of friction do not dominate the behavior at these strains. Eight-node biquadratic axisymmetric quadrilateral elements with reduced integration (CAX8R) were used in all the simulations and the element size was approximately 0.1 mm in all models.

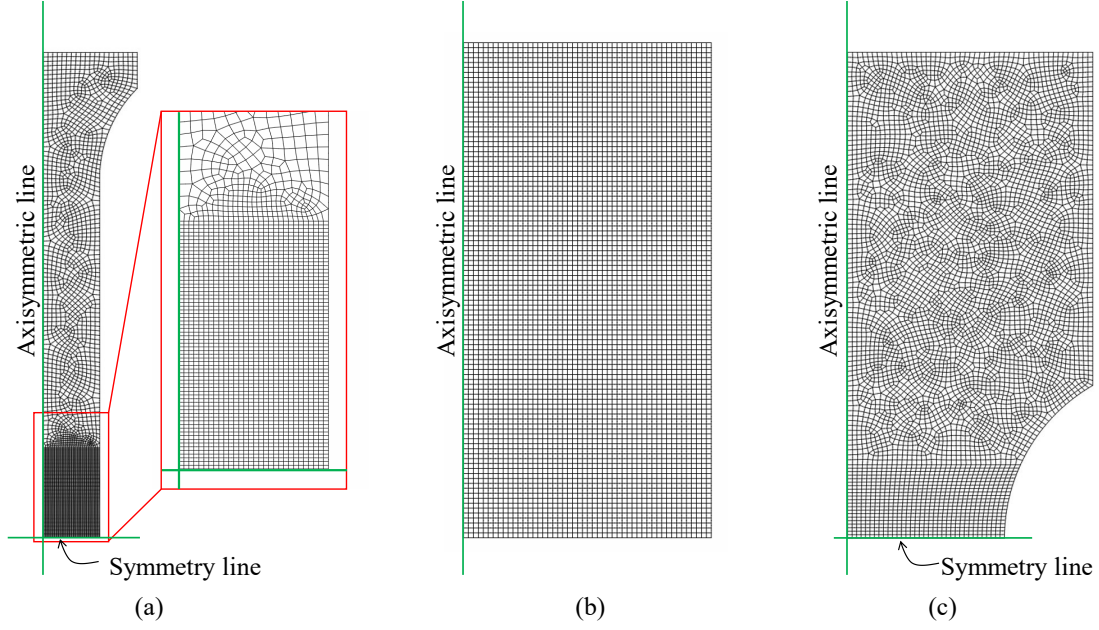


Figure 7: Finite element models used in the numerical simulations: (a) Uniaxial tension specimen, (b) upsetting specimen, and (c) pre-notched diabolo specimen.

Work hardening is represented by an extended Voce hardening rule that reads

$$\sigma_Y(p) = A + \sum_{i=1}^2 Q_i (1 - \exp(-C_i p)) \quad (18)$$

where σ_Y is the quasi-static flow stress in tension, p is the equivalent plastic strain, A represents the initial yield stress, while Q_i and C_i are parameters controlling the shape of the hardening curve. The parameters A , Q_1 , C_1 , Q_2 , and C_2 are tabulated in Table 7 and were all, except for AA6070-T4, determined by curve-fitting Eq. (18) to the flow-stress curves from uniaxial tension tests. The hardening curves were introduced into Abaqus/Standard in tabular form with 100 data points for equivalent plastic strains from 0 to 0.6. For equivalent plastic strains above 0.6, the solver assumes perfect plasticity. In practice, this means that the flow stress saturates at a plastic strain of 0.6 which should be adequate since the highest strain value reported in this study is approximately 0.25. To illustrate the diversity of the flow stress behavior of the different materials Figure 1 shows the flow stress curves approximated by Eq. (18). Note that the curve for 6070-T4 is based on the quasi-static flow stress in compression, as opposed to tension as it is for the other materials. This is accounted for in Abaqus/Standard by defining the plasticity curve as a compression curve instead of a tension curve which slightly changes the formulation of the Drucker-Prager yield criterion (Abaqus

Table 7: Parameters of the isotropic extended Voce hardening rule.

Configuration	A (MPa)	Q_1 (MPa)	C_1	Q_2 (MPa)	C_2
6060-0	25.0	57.6	38.6	85.9	1.3
6060-T6	167.0	40.6	26.7	136.2	0.5
6060-T7	128.0	54.3	33.4	875.2	0.04
6070-0	50.5	80.4	41.5	90.4	2.6
6070-T4*	146.8	74.3	226.9	256.2	8.9
6070-T6	372.5	21.0	217.7	75.1	6.8
6070-T7	341.0	32.5	38.9	33.0	3.2
6082.25-0	55.0	65.5	54.4	103.0	2.4
6082.25-T6	323.0	55.8	14.2	161.5	0.5
6082.25-T7	174.0	74.8	34.8	1118.9	0.06
6082.50-0	27.0	59.8	60.0	109.0	3.2
6082.50-T6	318.0	74.2	10.6	-	-
6082.50-T7	203.0	71.2	28.9	-	-

*Note that the parameters for 6070-T4 are determined from an upsetting test, and thus represent the quasi-static flow stress in compression.

[Documentation, 2014](#)).

5.4. Simulation results

Figure 8 compares true stress-strain curves from simulations of AA6070 with the pressure insensitive von Mises yield surface to the pressure sensitive Drucker-Prager yield surface. The compression tests in Figure 8a were simulated with frictionless interfaces between the test specimen and the platens, meaning that these results merely confirm that the von Mises yield surface predicts the same response in compression and tension and that the Drucker-Prager surface does not. Figure 8b shows that geometrical effects are minor since the compressive and tensile stresses are practically equal in the von Mises simulations of pre-notched diabolo geometry. This means that the observed SD effect is not a geometric artifact. Further, the practical implication of the pressure dependence of the Drucker-Prager model reveals itself here. Since the uniaxial tension tests were used to calibrate tempers O, T6, and T7, the Drucker-Prager model predicts identical axial stresses to the von Mises model for this specimen geometry. Similarly, the upsetting test was used to calibrate AA6070-T4, and the Drucker-Prager result is identical to the von Mises result for this configuration. In accordance with the experimental data, the Drucker-Prager model predicts higher stresses in the upsetting tests than for uniaxial tension tests for tempers T4, T6, and T7, while there is almost no

difference for temper O. Since the pre-notched diabolo tensile test has a higher stress triaxiality ratio than the corresponding uniaxial tests the axial stresses are lower using the Drucker-Prager yield criterion than the von Mises criterion. Conversely, for the compression tests the Drucker-Prager yield criterion predicts higher axial stresses in compression than the von Mises yield criterion.

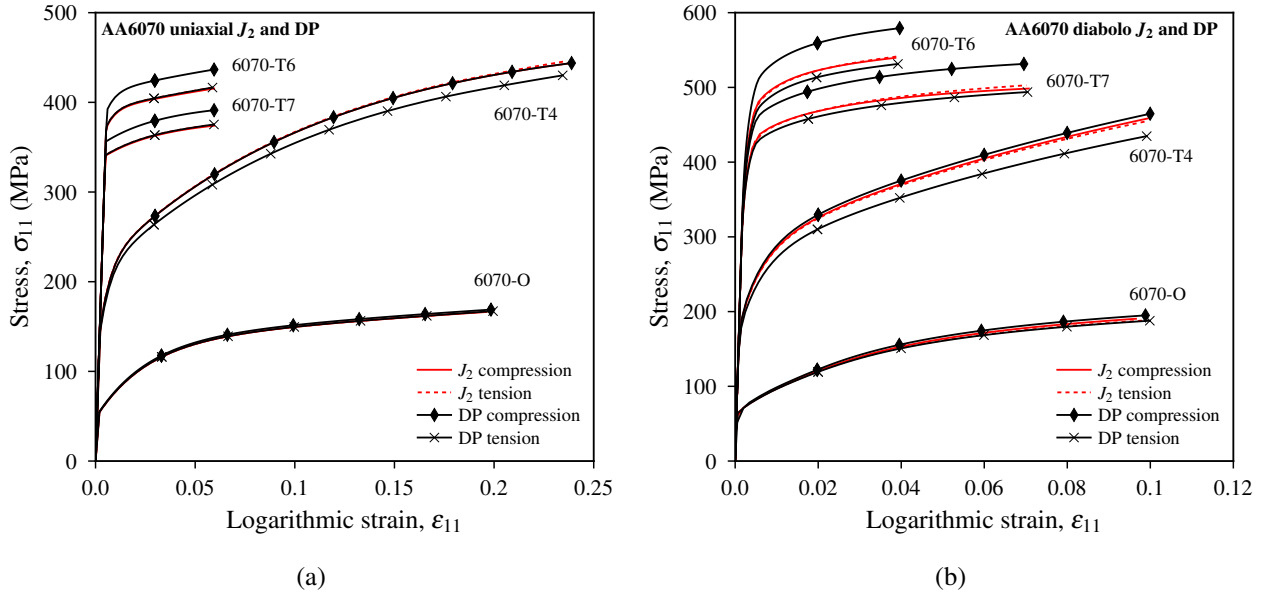


Figure 8: True stress-strain curves from simulations with the von Mises (J_2) and Drucker-Prager (DP) models for (a) uniaxial tests and (b) pre-notched diabolo tests for aluminum alloy AA6070.

Figure 9 shows the numerical simulations from Figure 8a alongside the representative experimental curves. As expected, the simulations correlate with the tests their material models were calibrated from. Further the Drucker-Prager simulations predict approximately the correct magnitude of the SD effect. Figure 10 and Figure 11 show the simulation results compared to experimental data for pre-notched diabolo specimens. To compare the entire data set to the simulations, results from every test are plotted in diffuse red for tension and diffuse gray for compression. In general, Figure 10 shows that the von Mises results are close to, but slightly above the test results in tension and significantly below the test results in compression except for 6082.25. The von Mises yield surface cannot capture the behavioral trends of the pre-notched diabolo tests.

Numerical simulations of pre-notched diabolo specimens with the Drucker-Prager model in Figure 11 show that due to the low stress levels, the SD effect for temper O are low in the simulations of all alloys, just as in the experiments. For the AA6070, AA6082.25, and AA6082.50 alloys, the magnitude of the SD

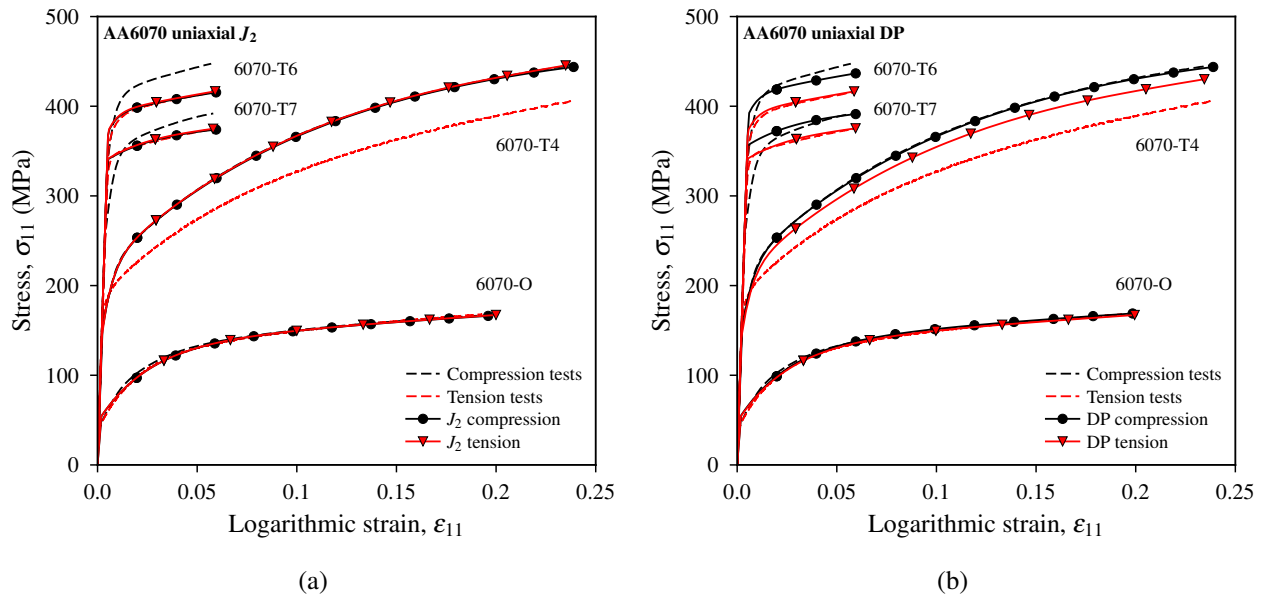


Figure 9: Simulations of uniaxial specimens for 6070 compared to the experimental tests: (a) von Mises (J_2) and (b) Drucker-Prager (DP) model. Note that the hardening for 6070-T4 is from a uniaxial compression test and that 6070-T4 was not fully developed when the uniaxial tensile test were conducted.

effect for temper T6 and temper T7 is also captured. However, the predicted stress levels for AA6082.25 are generally too high. We attribute this discrepancy to the anisotropy of the material. The experimental results show that AA6082.25 exhibits a higher axial stress in uniaxial tension than AA6082.50, while it is the other way around for the pre-notched diabolo tension tests, indicating that the isotropic model cannot fully predict the material behavior. For aluminum alloy AA6060, the SD effect is underestimated for T6 and T7 meaning that the pressure sensitivity of this alloy is larger than predicted by Eq. (16).

6. Discussion

As discussed in the introduction of the paper, several explanations for the SD effect have been postulated in the last decades. In the majority of our experiments there is a clear difference between the axial stresses in compression and tension. This difference seems to increase with the yield strength of the material which indicates that aluminum alloys are pressure sensitive. We conducted the modeling presuming that the difference between compressive and tensile stresses is due to effects of pressure on dislocation motion. In other words, we presumed that [Spitzig and Richmond](#)'s proposition is correct. This presumption accounts for parts of the observed SD effect. However, the discrepancies between modeling and experiment in Figure

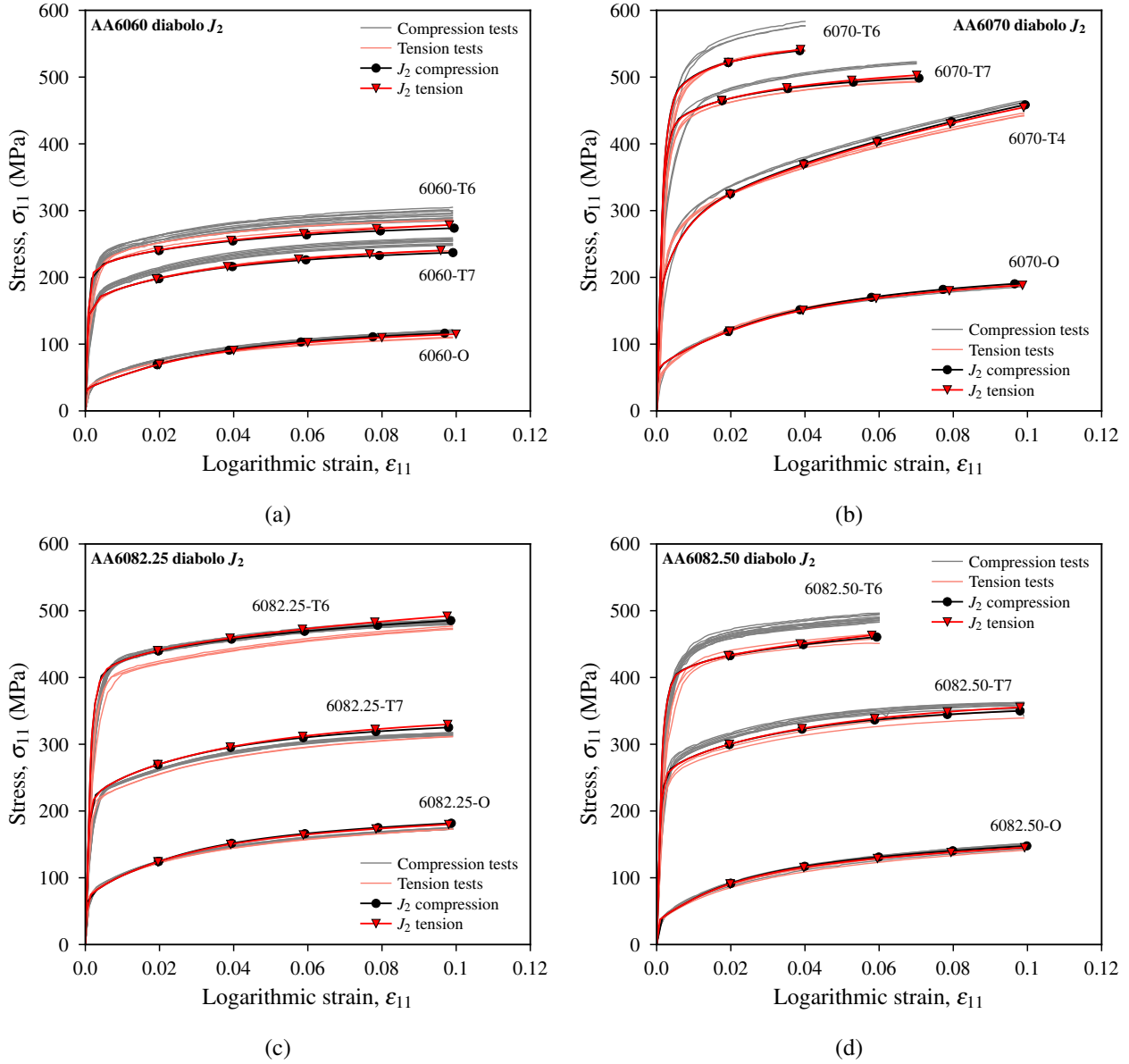


Figure 10: Simulations of pre-notched diablo specimens with the von Mises (J_2) yield surface compared to the experimental tests: (a) 6060, (b) 6070, (c) 6082.25, and (d) 6082.50.

9b and Figure 11 show that this near-linear relationship between axial stress and SD effect does not provide the complete explanation. Figure 12 shows the friction angles β calculated from Eq. (16) as a black dashed line that increases with the stress. The friction angle represents the pressure sensitivity of the material, and the dashed line represents the input to the numerical simulations that were presented in Section 5. Table 6 provides the corresponding β -values. The experimentally determined maximum, average, and

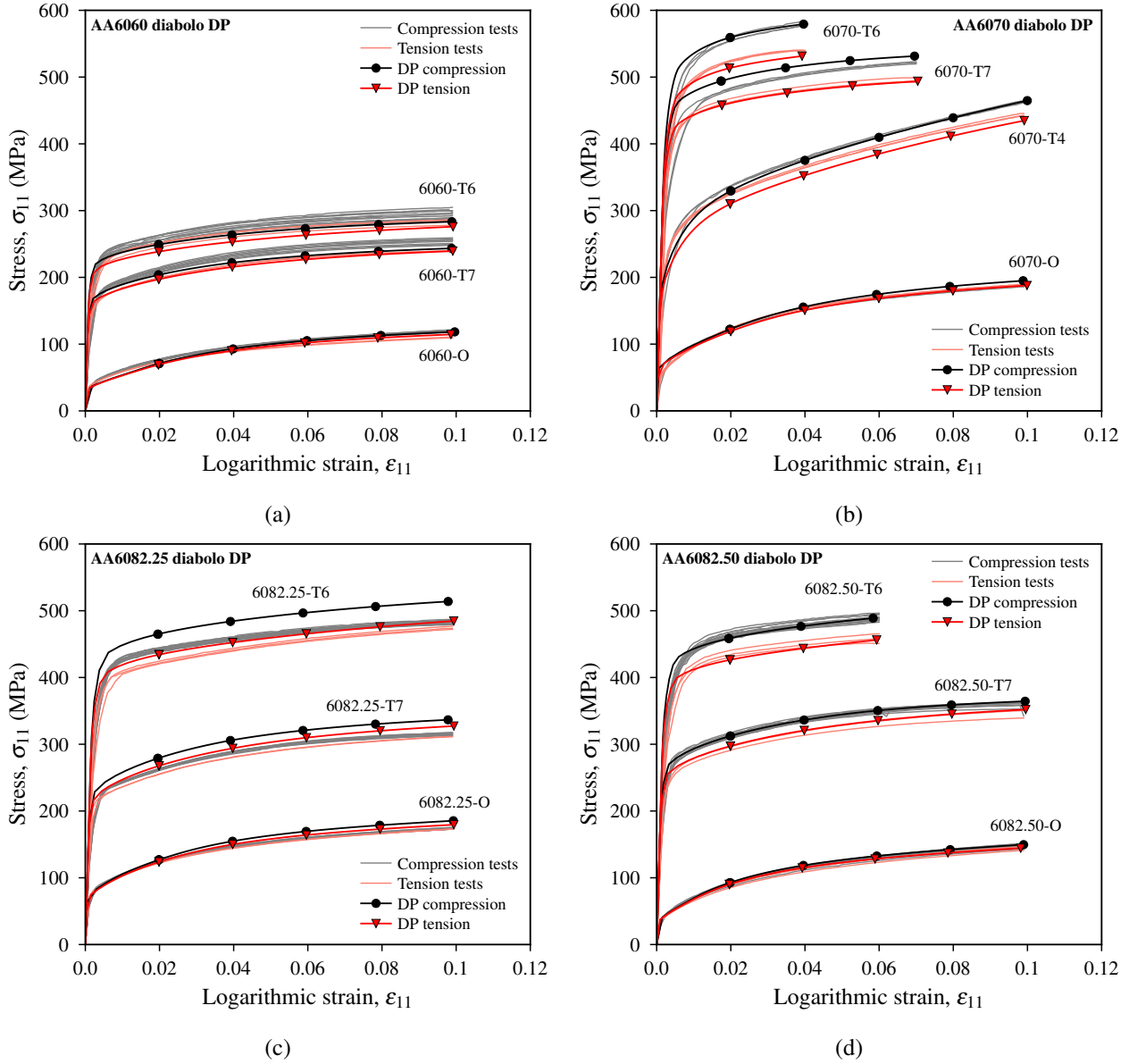


Figure 11: Simulations of pre-notched diabolo specimens with the Drucker-Prager (DP) yield surface compared to the experimental tests: (a) 6060, (b) 6070, (c) 6082.25, and (d) 6082.50.

minimum friction angles β calculated using Eq. (15) are plotted as markers in Figure 12. Here, the values are provided in Table 4. The solid lines illustrate the trends of the different alloys. The friction angles for AA6060 and AA6082.50 are underestimated by Eq. (16), but the predictions for AA6070 and AA6082.25 are good. These results show that the compressive stress is higher than the tensile stress in age hardened 6xxx aluminum alloys which, again, strongly suggest that AA6xxx aluminum alloys are pressure sensitive.

However, the discrepancies between the tests and the model indicate that other factors also come into play.

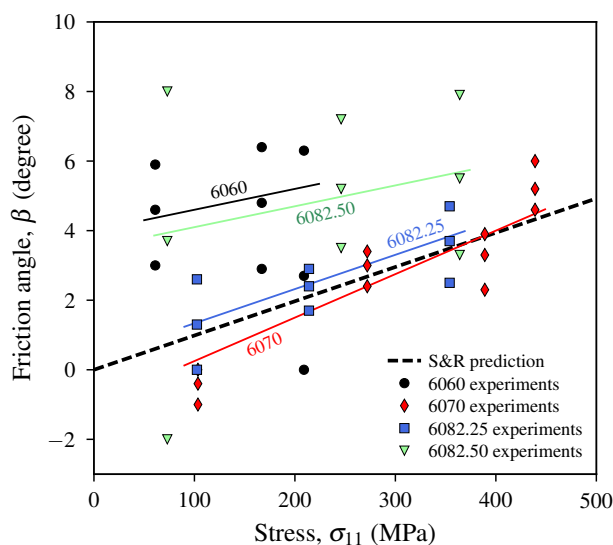


Figure 12: Friction angle β plotted against axial stress σ_{11} at a logarithmic strain of 0.02 for every material configuration. The dashed line represents the [Spitzig and Richmond \(1984\)](#) (S&R) prediction from Eq. (16). The point markers are the maximum, average, and minimum friction angles determined from the experiments (Table 4). The solid trend lines are drawn to aid the eye.

[Bai and Wierzbicki \(2008\)](#) previously conducted a study similar to ours for aluminum alloy AA2024-T351, but they also incorporated the effect of the Lode parameter by conducting plane strain tension tests. From these tests they saw that changing the Lode parameter from -1 to 0 affected the results significantly, but when the Lode parameter changed sign, that is when the stress state went from axisymmetric tension ($L_\mu = -1$) to axisymmetric compression ($L_\mu = 1$), the pressure sensitivity governed. Thus, our work confirms with significant experimental evidence the results of [Bai and Wierzbicki \(2008\)](#). These results considered in light of the study of [Spitzig and Richmond \(1984\)](#) who varied the hydrostatic pressure while keeping the Lode parameter constant, indicate that aluminum is pressure sensitive and that this type of SD effect is not a result of tension-compression asymmetry in the deviatoric plane. The results also confirm the experimental results of [Wilson \(2002\)](#). He obtained similar simulation results with an associative Drucker-Prager model and a similar pressure sensitivity parameter as we did in this study.

When modeling notched tension tests with a pressure independent yield surface, the stress level is often overestimated. This overestimation of the stress level in pre-notched tensile tests can be substantially reduced by using anisotropic plasticity models as shown in [Fourmeau et al. \(2011\)](#). The overestimation can also be reduced by using porous plasticity models ([Westermann et al., 2014](#)), but since the initial void-volume fraction is usually small and that voids close in compression, the effect of porous plasticity is minor.

It appears that neither anisotropy nor void growth can explain the entire difference which again suggests pressure dependence.

The SD effect was by [Fourmeau et al. \(2011\)](#) found to be a function of the orientation of the test specimens, meaning that it matters if the specimen is extracted from the rolling/extrusion direction or the transverse direction. In the current study, AA6070 in uniaxial conditions exhibits the same trend in all orientations. However, the pre-notched diabolo tests were only extracted from the rolling direction for AA6070, and only from the transverse direction for the other alloys.

Our experiments were conducted for materials with different crystallographic textures and grain structures: AA6060 is recrystallized with equiaxed grains, AA6082.25 is non-recrystallized with pancake-shaped grains and sub-grains, AA6082.50 and AA6070 are recrystallized with large elongated grains. We know from previous studies that plastic anisotropy induced by the crystallographic texture influences the plastic deformation and stress distribution during necking of a tension test. The different crystallographic textures and thus different plastic anisotropy of the alloys have affected the results in this study. We also expect that there has been some influence from the differences in grain size. In further work, it would be of great interest to perform tension and compression tests on aluminum alloys of different strengths with random texture, isotropic behavior, and equiaxed and equal-sized grains. This way the significance of plastic anisotropy and grain structure could be removed and the effect of hydrostatic pressure isolated.

The main implication of the SD effect is that the classical J_2 flow theory where the plastic behavior of the material is independent of the hydrostatic stress cannot be used to obtain accurate results even in engineering applications. The buckling capacity of columns can for example be underestimated if the SD effect is not taken into account. Due to the SD effect, the stress level in notched tensile tests are often overestimated in numerical simulations. [Kuwabara \(2007\)](#) highlights that accurate predictions of metal forming processes are dependent on knowledge of the SD effect. Pressure dependence will also affect the stress distribution in specimens at various stress triaxiality ratios and thus the point of incipient fracture, making it important in ductile fracture modeling.

7. Concluding remarks

There is a discrepancy between the measured compressive and tensile stress-strain curves for nearly all the material tests presented in this paper. This strength differential (SD) effect was in some cases as large as 6.3% and the magnitude increased with increasing stress, suggesting that AA6xxx-series aluminum alloys

are pressure dependent. Our results are consistent with other results on aluminum alloys from the literature and indicate that the macroscopic pressure dependence can be a consequence of the effect of pressure on dislocation motion.

Numerical simulations with the pressure independent von Mises yield surface are only capable of reproducing the uniaxial tests that were used for calibration. At higher stress triaxiality ratios (lower pressures) the von Mises results overestimate the axial stress, and at lower stress triaxiality ratios (higher pressures) the von Mises results underestimate the axial stress. The pressure dependent yield surface of Drucker and Prager assumes that yielding of the material is linearly dependent on the pressure. By calculating the pressure dependence from a presumption that dislocation motion is affected by the pressure as suggested by [Spitzig and Richmond \(1984\)](#), numerical simulations using the Drucker-Prager yield surface correctly predict the trends seen in the experiments. This particular approach to the model requires no additional tests for calibration compared to the von Mises model.

We can say with some certainty that yielding of aluminum alloys is pressure dependent. The importance of the third invariant of the stress tensor J_3 has been highlighted in literature but the main reason for the SD effect observed in this study is most likely not J_3 -dependence. However, the plastic anisotropy and grain structure of the investigated materials can have influenced the SD effect; this requires additional work. Accurately determining the SD effect in a uniaxial condition is difficult due to the friction between the test specimens and the machine platens in upsetting tests, and this might obscure experimental results. In this study we observed SD effects in pre-notched diabolo test specimens which do not suffer the same problems as the uniaxial upsetting test.

Acknowledgment

The financial support for this work comes from the Centre for Advanced Structural Analysis (SFI CASA).

References

- Abaqus Documentation, 2014. Abaqus Analysis User's Guide, Version 6.14. Dassault Systemès Simulia Corp., Providence, RI, USA.
- Abaqus/Standard, 2014. Version 6.14. Dassault Systemès Simulia Corp., Providence, RI, USA.
- Bai, Y., Wierzbicki, T., 2008. A new model of metal plasticity and fracture with pressure and Lode dependence. *International Journal of Plasticity* 24, 1071–96.
- Bridgman, P.W., 1944. The stress distribution at the neck of a tension specimen. *Transactions of the American Society of Metals* 32, 553–74.

- Bridgman, P.W., 1952. *Studies in Large Plastic Flow and Fracture*. McGraw-Hill, New York, NY, USA.
- Brüning, M., 1999. Numerical simulation of the large elastic-plastic deformation behavior of hydrostatic stress-sensitive solids. *International Journal of Plasticity* 15, 1237–64.
- Bulatov, V.V., Richmond, O., Glazov, M.V., 1999. An atomistic dislocation mechanism of pressure-dependent plastic flow in aluminum. *Acta Metallurgica* 4, 667–73.
- Cazacu, O., Barlat, F., 2004. A criterion for description of anisotropy and yield differential effects in pressure-insensitive materials. *International Journal of Plasticity* 20, 2027–45.
- Chait, R., 1972. Factors influencing the strength differential of high strength steels. *Metallurgical Transactions* 3, 365–71.
- Dieter, G.E., 1988. *Mechanical Metallurgy*. 3rd ed., McGraw-Hill, London, UK.
- Drucker, D.C., 1973. Plasticity theory, strength-differential (SD) phenomenon, and volume expansion in metals and plastics. *Metallurgical Transactions* 4, 667–73.
- Drucker, D.C., Prager, W., 1952. Soil mechanics and plastic analysis for limit design. *Quarterly of Applied Mathematics* 10, 157–65.
- Fourmeau, M., Børvik, T., Benallal, A., Lademo, O.G., Hopperstad, O.S., 2011. On the plastic anisotropy of an aluminium alloy and its influence on constrained multiaxial flow. *International Journal of Plasticity* 27, 2005–25.
- Frodal, B.H., Pedersen, K.O., Børvik, T., Hopperstad, O.S., 2017. Influence of pre-compression on the ductility of AA6xxx aluminium alloys. *International Journal of Fracture* 206, 131–49.
- Gao, X., Zhang, T., Hayden, M., Roe, C., 2009. Effect of the stress state on plasticity and ductile failure of an aluminum 5083 alloy. *International Journal of Plasticity* 25, 2366–82.
- Gao, X., Zhang, T., Zhou, J., Graham, S.M., Hayden, M., Roe, C., 2011. On stress-state dependent plasticity modeling: Significance of the hydrostatic stress, the third invariant of stress deviator and the non-associated flow rule. *International Journal of Plasticity* 27, 217–31.
- Guo, T.F., Faleskog, J., Shih, C.F., 2008. Continuum modeling of a porous solid with pressure-sensitive dilatant matrix. *Journal of the Mechanics and Physics of Solids* 56, 2188–212.
- Habib, S.A., Khan, A.S., Gnäupel-Herold, T., 2017. Anisotropy, tension-compression asymmetry and texture evolution of a rare-earth-containing magnesium alloy sheet, ZEK100, at different strain rates and temperatures: Experiments and modeling. *International Journal of Plasticity* 95, 163–90.
- Hancock, J.W., Mackenzie, A.C., 1976. On the mechanisms of ductile failure in high-strength steels subjected to multi-axial stress-states. *Journal of the Mechanics and Physics of Solids* 24, 147–69.
- Hirth, J.P., Cohen, M., 1970. On the strength-differential phenomenon in hardened steel. *Metallurgical Transactions* 1, 3–8.
- Holmen, J.K., Johnsen, J., Hopperstad, O.S., Børvik, T., 2016. Influence of fragmentation on the capacity of aluminum alloy plates subjected to ballistic impact. *European Journal of Mechanics A/Solids* 55, 221–33.
- Holmen, J.K., Johnsen, J., Jupp, S., Hopperstad, O.S., Børvik, T., 2013. Effects of heat treatment on the ballistic properties of AA6070 aluminium alloy. *International Journal of Impact Engineering* 57, 119–33.
- Hosford, W.F., Allen, T.J., 1973. Twinning and directional slip as a cause for a strength differential effect. *Metallurgical Transactions* 4, 1424–5.
- Johnsen, J., Holmen, J.K., Myhr, O.R., Hopperstad, O.S., Børvik, T., 2013. A nano-scale material model applied in finite element analysis of aluminium plates under impact loading. *Computational Materials Science* 79, 724–35.

- Khadyko, M., Dumoulin, S., Børvik, T., Hopperstad, O.S., 2014. An experimental-numerical method to determine the work-hardening of anisotropic ductile materials at large strains. *International Journal of Mechanical Sciences* 88, 25–36.
- Kleiser, G.J., Revil-Baudard, B., Cazacu, O., Pasiliao, C.L., 2015. Plastic deformation of polycrystalline molybdenum: Experimental data and macroscopic model accounting for its anisotropy and tension-compression asymmetry. *International Journal of Solids and Structures* 75-76, 287–98.
- Kuroda, M., 2004. A phenomenological plasticity model accounting for hydrostatic stress-sensitivity and vertex-type of effect. *Mechanics of Materials* 36, 285–97.
- Kuwabara, T., 2007. Advances in experiments on metal sheets and tubes in support of constitutive modeling and forming simulations. *International Journal of Plasticity* 26, 385–419.
- Lou, Y., Huh, H., Yoon, J.W., 2013. Consideration of strength differential effect in sheet metals with symmetric yield functions. *International Journal of Mechanical Sciences* 66, 214–23.
- Nixon, M.E., Cazacu, O., Lebensohn, R.A., 2010. Anisotropic response of high-purity α -titanium: Experimental characterization and constitutive modeling. *International Journal of Plasticity* 26, 516–32.
- Peng, J., Wu, P.D., Huang, Y., Chen, X.X., Lloyd, D.J., Embury, J.D., Neale, K.W., 2009. Effects of superimposed hydrostatic pressure on fracture in round bars under tension. *International Journal of Solids and Structures* 46, 3741–9.
- Seidt, J.D., Gilat, A., 2013. Plastic deformation of 2024-T351 aluminum plate over a wide range of loading conditions. *International Journal of Solids and Structures* 50, 1787–90.
- Singh, A.P., Padmanabhan, K.A., Pandey, G.N., Murty, G.M.D., Jha, S., 2000. Strength differential effect in four commercial steels. *Journal of Materials Science* 35, 1379–88.
- Smith, J., Liu, W.K., Cao, J., 2013. A general anisotropic yield criterion for pressure-dependent materials. *International Journal of Plasticity* 75, 2–21.
- Spitzig, W.A., Richmond, O., 1984. The effect of pressure on the flow stress of metals. *Acta Metallurgica* 32, 457–63.
- Spitzig, W.A., Sober, R.J., Richmond, O., 1975. Pressure dependence of yielding and associated volume expansion in tempered martensite. *Acta Metallurgica* 23, 885–93.
- Spitzig, W.A., Sober, R.J., Richmond, O., 1976. The effect of hydrostatic pressure on the deformation behavior of maraging and HY-80 steels and its implications for plasticity theory. *Metallurgical Transactions A* 7, 1703–10.
- Stoughton, T.B., Yoon, J., 2004. A pressure-sensitive yield criterion under a non-associated flow rule for sheet metal forming. *International Journal of Plasticity* 20, 705–31.
- Tuninetti, V., Gilles, G., Milis, O., Pardoën, T., Habraken, A.M., 2015. Anisotropy and tension-compression asymmetry modeling of the room temperature plastic response of Ti-6Al-4V. *International Journal of Plasticity* 67, 53–68.
- Westermann, I., Pedersen, K.O., Furu, T., Børvik, T., Hopperstad, O.S., 2014. Effects of particles and solutes on strength, work-hardening and ductile fracture of aluminum alloys. *Mechanics of Materials* 79, 58–72.
- Wilson, C.D., 2002. A critical reexamination of classical metal plasticity. *Journal of Applied Mechanics* 69, 63–8.
- Wu, P.D., Embury, J.D., Lloyd, D.J., Huang, Y., Neale, K.W., 2009. Effects of superimposed hydrostatic pressure on sheet metal formability. *International Journal of Plasticity* 25, 1711–25.
- Yoon, J.W., Lou, Y., Yoon, J., Glazoff, M.V., 2014. Asymmetric yield function based on the stress invariants for pressure sensitive materials. *International Journal of Plasticity* 56, 184–202.